
Article:
García-Peris, MÁ, Ruiz, G., Kubota, S. et al. (2025) Opportunities and challenges to study solar neutrinos with a Q-Pix pixel readout. Physical Review D, 112. 092009. ISSN: 2470-0010

https://doi.org/10.1103/xq7l-lv7j

Opportunities and challenges to study solar neutrinos with a Q-Pix pixel readout

M. Á. García-Peris,[1,*] G. Ruiz,[1] S. Kubota,[1,2,3] A. Navrer-Agasson,[4] G. V. Stenico,[5] E. Gramellini,[1] R. Guenette,[1] J. Asaadi,[6] J. B. R. Battat,[7] V. A. Chirayath,[6] E. Church,[8] Z. Djurcic,[9] A. C. Ezeribe,[10] J. N. Gainer,[6] G. Gansle,[6] K. Keefe,[6] N. Lane,[1] C. Mauger,[11] Y. Mei,[6] F. M. Newcomer,[11] D. R. Nygren,[6] M. Rooks,[6] P. Sau,[6] O. Seidel,[6] S. Söldner-Rembold,[4] I. Tzoka,[6] and R. Van Berg[11]

[1]*Department of Physics and Astronomy, University of Manchester, Manchester M13 9PL, United Kingdom*
[2]*Department of Physics, Harvard University, Cambridge, Massachusetts 02138, USA*
[3]*Lawrence Berkeley National Laboratory, Berkeley, California 94720, USA*
[4]*Department of Physics, Imperial College London, London SW7 2AZ, United Kingdom*
[5]*School of Physics and Astronomy, University of Edinburgh, Edinburgh EH8 9YL, United Kingdom*
[6]*Department of Physics, University of Texas at Arlington, Arlington, Texas 76019, USA*
[7]*Department of Physics and Astronomy, Wellesley College, Wellesley, Massachusetts 02481, USA*
[8]*Pacific Northwest National Laboratory, Richland, Washington 99354, USA*
[9]*Argonne National Laboratory, Lemont, Illinois 60439, USA*
[10]*School of Mathematical and Physical Sciences, University of Sheffield, Sheffield, S3 7RH, United Kingdom*
[11]*Department of Physics and Astronomy, University of Pennsylvania, Philadelphia, Pennsylvania 19104, USA*

(Received 24 July 2025; accepted 22 October 2025; published 17 November 2025)

The study of solar neutrinos presents significant opportunities in astrophysics, nuclear physics, and particle physics. However, the low-energy nature of these neutrinos introduces considerable challenges to isolate them from background events, requiring detectors with low-energy threshold, high spatial and energy resolutions, and low data rate. We present the study of solar neutrinos with a kiloton-scale liquid argon detector located underground, instrumented with a pixel readout using the Q-Pix technology. We explore the potential of using volume fiducialization, directional topological information, light signal coincidence, and pulse-shape discrimination to enhance solar neutrino sensitivity. We find that discriminating neutrino signals below 5 MeV is very difficult. However, we show that these methods are useful for the detection of solar neutrinos when external backgrounds are sufficiently understood and when the detector is built using low-background techniques. When building a workable background model for this study, we identify γ background from the cavern walls and from capture of α particles in radon decay chains as both critical to solar neutrino sensitivity and significantly underconstrained by existing measurements. Finally, we highlight that the main advantage of the use of Q-Pix for solar neutrino studies lies in its ability to enable the continuous readout of all low-energy events with minimal data rates and manageable storage for further off-line analyses.

DOI: 10.1103/xq7l-lv7j

I. INTRODUCTION

Solar neutrinos have historically played a fundamental role in both particle physics and astrophysics and they continue to attract the attention of the physics community today. The solar neutrino flux arises from the different nuclear fusion reaction chains occurring in the Sun's core. It is predicted by the Standard Solar Model (SSM) [1,2], a framework that also describes the mechanisms of energy production, internal structure, and evolution of the stars.

The first attempt to study the solar neutrino flux in 1968 led to the solar neutrino problem and the subsequent discovery of neutrino oscillations [1,3–5]. As neutrinos propagate through the dense solar medium, Mikheyev-Smirnov-Wolfenstein matter effects have a significant impact on the oscillation effect [6]. This makes solar neutrinos a powerful probe to accurately measure oscillation parameters, including mass-squared differences and mixing angles [7]. Today, the long-standing tension between solar and reactor

*Contact author: miguel.garciaperis@manchester.ac.uk

measurements of Δm^2_{21} remains unresolved, with the KamLAND reactor experiment reporting a best-fit value approximately 1.5 standard deviations higher than that inferred from solar neutrino data [8,9].

Beyond for neutrino physics, solar neutrinos provide a rich testing ground for the SSM itself. The characterization of the different components of the solar neutrino flux has validated the SSM predictions and continues to offer a way to refine our understanding of the Sun. Recent spectroscopic measurements of the Sun's metallicity [10,11], defined as the fraction of the solar mass consisting of elements heavier than helium, are in tension with earlier helioseismology results [12] that had been consistent with the SSM. This discrepancy, known as the solar metallicity problem, could be resolved by precise measurements of neutrino flux from the carbon-nitrogen-oxygen (CNO) cycle, since higher metallicity enhances CNO neutrino production.

Despite the large flux of solar neutrinos [13], their small interaction cross section and the resulting low-energy signals make their detection a significant experimental challenge. Most solar neutrinos are produced below 1 MeV, where the pp chain dominates, followed by contributions from the CNO cycle and the monoenergetic Be7 lines. Above 1 MeV, B8 and the not yet observed hep neutrinos are the most abundant. With the exception of monoenergetic pep line at ∼1.5 MeV, the flux above 1 MeV peaks around 10 MeV and fades at 20 MeV, which is significantly lower than the typical energies of accelerator neutrinos (ranging from tens of MeVs to GeVs) and even supernova neutrinos (up to 50 MeV [14]). These low-energy signals demand detectors with very low energy-detection thresholds, extremely low background levels, and excellent reconstruction capabilities.

Scintillator neutrino detectors such as Borexino [15] and SNO+ [16] have achieved very low energy-detection thresholds, with Borexino operating above 0.2 MeV and SNO+ expected to operate above the range [0.5,1.0] MeV. Borexino has reported measurement of the pp flux [17], the pep and Be7 fluxes [18], the B8 flux [19], and has provided the first measurement of the CNO flux [20,21]. SNO+ has already reported on the B8 flux [22], and it is expected to provide complementary measurements of the CNO flux to those of Borexino. The water-Cherenkov detector Super-Kamiokande (SK) [23] has a higher energy threshold for solar neutrino detection (in the range [3.5,4.0] MeV), but its large fiducial mass and exposure have allowed the accumulation of high-statistics solar neutrino samples. This has enabled studies of night-day asymmetry in the neutrino flux, the neutrino oscillation parameters, the existence of an "upturn" in the electron neutrino survival probability, and to perform searches of hep neutrinos [24].

Multipurpose next-generation neutrino detectors also aim to study solar neutrinos. Hyper-Kamiokande (HK) is not expected to lower SK's energy threshold, but its larger fiducial mass will allow further refinement of SK's B8 studies and potentially the observation of hep flux after a few decades of data taking [25]. The liquid scintillator experiment JUNO [26], with a sub-MeV energy detection threshold, will contribute to the precise characterization of the CNO, pep, Be7, and B8 fluxes [27]. On the other hand, liquid-argon time-projection chamber (LArTPC) technology has repeatedly been identified as an ideal approach to perform comprehensive analyses of the B8 and hep fluxes [28,29]. This is due to its excellent energy and spatial resolution, as well as its ability to separate different interaction channels, providing nondegenerate access to neutrino oscillation parameters. Achieving this potential requires sufficient fiducial mass, effective background control, and enhanced detection techniques, which this study addresses for the first time.

LArTPCs have been widely used in neutrino experiments like ICARUS [30], MicroBooNE [31], and several others [32–34], usually in an accelerator context. Their use in low-energy searches has been limited by the intrinsic argon radioactivity, which sets a detection threshold above 5 MeV [35] and, in practice, demands an almost continuous readout to ensure that rare low-energy signals are not discarded. LArTPC historically rely on projective charge readouts, where ionization charge is detected using consecutive layers of wire planes bonded over Anode Plane Assemblies (APA). The two spatial coordinates perpendicular to the charge drift direction are reconstructed by interpolating the signals of the wires, while the absolute position along the drift direction is inferred from the trigger time. Projective readouts are subject to reconstruction ambiguities for events with complex, dense topologies [36], and the wire spacing imposes a physical limit on both spatial and energy resolution, which is critical to identify low-energy signals. Furthermore, the long sensing wires introduce a capacitive load that adds noise to the readout electronics, potentially rising the effective energy threshold [37].

Scaling such readouts, which are mounted on large and heavy support structures [38], to large-scale detectors implies significant engineering complexity. Moreover, increasing the drift distance requires longer readout windows, which along with the intrinsic backgrounds of the argon, raises the data rates of the experiment. Charge readout planes (CRPs) [39] haven been proposed to mitigate some of these issues. CRPs are modular, mechanically robust assemblies of stacked, segmented, and perforated printed circuit boards (PCBs) with etched electrodes, suitable for large-scale production. While CRPs simplify construction and improve robustness, the readout remains intrinsically projective. Therefore, the limitations related to reconstruction ambiguities, the electronic noise and the data rates, persist.

A natural solution to these limitations comes from pixelated readouts, which maintain mechanical robustness while providing fine spatial and energy resolution, as well as unambiguous event reconstruction in three dimensions. These capabilities are particularly relevant for solar

neutrino studies: the reconstructed event direction with respect to the Sun can be used to suppress backgrounds and to separate neutrino interaction channels, while improved energy resolution enables the separation of B8 and hep contributions to the solar neutrino spectrum. However, instrumenting a kilotonne-scale LArTPC with a pixelated readout requires $\mathcal{O}(10^8)$ channels, which again implies major challenges in terms of data rate and power consumption. Research collaborations worldwide, such as LArPix [40,41], SoLAr [42], and Q-Pix [43], have been working to enable large-scale LArTPCs equipped with fully pixelated, low-power charge readout, opening the path toward high-precision solar neutrino measurements.

The Q-Pix technology offers several advantages. Its continuous readout architecture [43] naturally solves the continuous readout necessity and, at the same time, suppresses data volumes by recording only charge arrival times, resulting in a substantially lower data rate compared to traditional projective readouts. This enables the storage of a much larger fraction of low-energy events for off-line analysis which, ultimately, makes it possible to push the detection threshold below that of projective readouts and even lower than water-Cherenkov detectors such as HK.

This work provides the first comprehensive study of the capabilities of an underground large-scale pixelated LArTPC detector to study solar neutrinos, particularly the B8 and hep chains, with the most comprehensive review of the background sources. We address this question under two detector scenarios: a multi-kt LArTPC module not optimized for low background (*high-background scenario*) and a module specifically designed to reduce backgrounds as outlined in the SLoMo detector proposal [44] (*low-background scenario*). The Q-Pix readout is used in both cases.

II. EXPERIMENTAL DESIGN ASSUMPTIONS

We outline here our assumptions regarding the experimental setup under study, the detector characteristics, and the host cavern.

A. Detector

High-background scenario. In the high-background scenario, we consider a state-of-the-art 17.5 kiloton LArTPC with 10 kiloton fiducial volume filled with atmospheric liquid argon hosted in a cryostat akin to [38] with no dedicated background mitigation arrangements. The dimensions of the fiducial volume are $(14.0 \times 12.0 \times 58.2)$ m^3, divided into four 3.5 m long drift volumes, as presented in Fig. 1. The clearances between the detector and the cryostat are 0.5 m in the drift direction, 1 m in the vertical axis, and 1.9 m in the longitudinal axis (respectively left-right, up-down and into–out-of page in Fig. 1). The electric field applied to the drift volumes is 500 V/cm. The collection planes are readout by contiguous Q-Pix pixels, supported by a lightweight mechanical structure. This design ensures minimal engineered structure and materials.

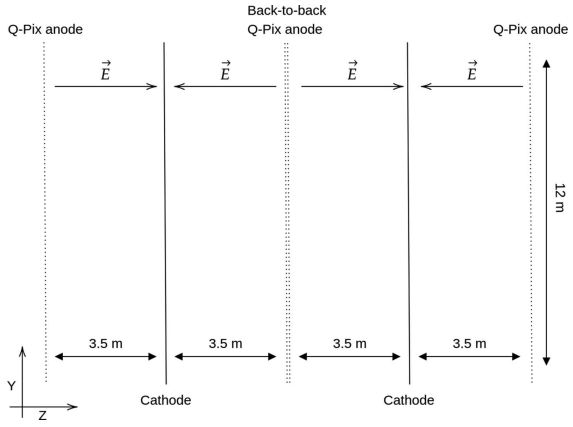

FIG. 1. Schematic cross-section view of the detector model with four drift volumes of 3.5 m each. The innermost Q-Pix anode plane consists of two pixel planes. The Z axis runs parallel to the planes, one facing each drift volume (not to scale).

In order to study the impact of light detection, we assume that the entire anode plane is sensitive to photons, which corresponds to a geometric coverage of 37% and we assume a 15% quantum efficiency to reflect the efficiency of currently available commercial solutions for photon detection at 128 nm [45]. This approach is in line with an innovative solution for light readouts that could offer high detection coverage if the pixels were sensitive to both charge and light [46,47]. Given that traditional photon coverage in LArTPCs is typically 3%–15% [38,39], this scenario is admittedly ambitious. The product of optical coverage and detection efficiency is 5 times larger than other proposals [48]. Nevertheless, this optimistic assumption serves as a benchmark to understand how photon detection could enhance solar neutrino detection in LArTPCs.

Low-background scenario. For the low-background scenario, we follow the SLoMo design [44]. The detector is akin to the high-background scenario, i.e., same readout systems and active volume but, in this case, filled with underground argon (UAr). An additional neutron absorber (either a water shield or a borated cryostat) is assumed to reduce the neutron contributions by 4 orders of magnitude and the radon background is suppressed by 3 orders of magnitude with dedicated argon recirculation and purification systems. These assumptions, although very optimistic, have been demonstrated by simulations and achieved by other experiments, as it will be described in the following sections.

B. Cavern

Neutrino detectors need to be located underground to be significantly shielded from backgrounds resulting from cosmic rays. Despite the suppressed cosmic-ray rates

underground, several backgrounds remain and depend on the characteristics of the cavern where the detector is located, such as the rock composition. For both the high- and low-background scenarios, we consider a cavern where the average composition of the rock is taken from Ref. [29].

III. THE Q-PIX READOUT, ITS SIMULATION, AND RECONSTRUCTION

The Q-Pix scheme employs zero suppression, self-triggering pixels, and dynamically established data networks to capture ionization signals in kiloton underground LArTPCs. A comprehensive review of the system can be found in Ref. [43]. Pixels remain in a low-power quiescent state until a predefined charge threshold ΔQ is reached, resetting the pixel and providing an 8-bits timestamp. The time difference between resets Δt is used to reconstruct the ionization charge deposited by charged particles in the detector, as presented in Ref. [49], ultimately enabling full event reconstruction. This approach ensures high-precision sampling of low-energy depositions while minimizing heat dissipation and data rates.

The response of the Q-Pix readout is simulated with two main packages:

(1) QPixG4: a Geant4 v4.11 [50] application with the FTFP_BERT_HP physics library, combined with the low energy generator MARLEY [51] and the neutrino interaction generator GENIE [52].
(2) QPixRTD: a stand-alone code that transforms the Geant4 output into Q-Pix resets, simulating the response of an anode plane fully tiled in (4×4) mm^2 contiguous pixels.

Background events are produced with custom-made generators, and solar neutrino events are generated by MARLEY [51]. The events are then run with the QPixG4 package, which produces energy deposits in space and time (hits). For simplicity, only $1/150$ of the volume of the detector is simulated, as the events are spatially small. Hits are then passed to QPixRTD, which simulates charge transport and converts collected charge into pixel resets. The optimization of this procedure is described in Ref. [53]. In practice, if the accumulated charge in a pixel does not reach the reset threshold, no reset occurs and the collected charge remains until a new charge deposition reaches the threshold. However, this effect is expected to be small and thus not considered in this work.

The event reconstruction is done by applying the density-based spatial clustering (DBSCAN) algorithm [54] over the reset spatial and temporal distribution, allowing to identify events of interest. It determines clusters depending on a predefined minimum number of resets, denoted as cluster threshold (CT), and a maximum separation ϵ between clusters. Considering the different nature of the x and y coordinates and the temporal coordinate, resets are first clustered on the pixel plane, where they are required to be contiguous, and afterwards along the temporal coordinate. Through this study, ϵ is fixed at 3 μs, equivalent to 5 mm, as this value was found optimal for depositions in the MeV energy range [53]. The value of CT will be determined in the following sections.

TABLE I. Expected total number of electron-neutrino interactions from the B8 and hep processes for charged-current (CC) and electron elastic scattering (ES) in 10 kiloton LAr active volume per year.

Interaction channel	Events/(10 kton × year)
B8 CC ($\nu_e + {}^{40}\mathrm{Ar} \to e^- + {}^{40}\mathrm{K}^*$)	14,380
B8 ES ($\nu_e + e^- \to \nu_e + e^-$)	9160
hep CC ($\nu_e + {}^{40}\mathrm{Ar} \to e^- + {}^{40}\mathrm{K}^*$)	86
hep ES ($\nu_e + e^- \to \nu_e + e^-$)	23

The collected charge can be reconstructed from the number N of resets produced, i.e., $Q_{\mathrm{rec}} = N \times \Delta Q$. However, since ΔQ is not infinitesimally small, some deposited charge may be lost when Q_{dep} is not an integer multiple of ΔQ. That is, $Q_{\mathrm{dep}} \geq N \times \Delta Q$ and, therefore, $Q_{\mathrm{dep}} \geq Q_{\mathrm{rec}}$, resulting in Q_{rec} being not entirely linear with N and Q_{dep}. While nontriggered quanta could degrade the charge collection, their impact can be mitigated by energy calibration and by the optimization of the reset threshold ΔQ. For low-energy neutrinos of the order of a few MeV, $\Delta Q = 1fC$ (6250 electrons) was found optimal [53]. Considering the argon W value of 23.6 eV [55], this is equivalent to 0.14 MeV, which constitutes the energy floor of the detector.

IV. SOLAR NEUTRINO PREDICTION

In this study, we target the detection of solar neutrinos produced either by the boron-8 (B8) process or the proton-proton IV (hep) process interacting in the detector via either charged current (CC) interaction or elastic scattering (ES)

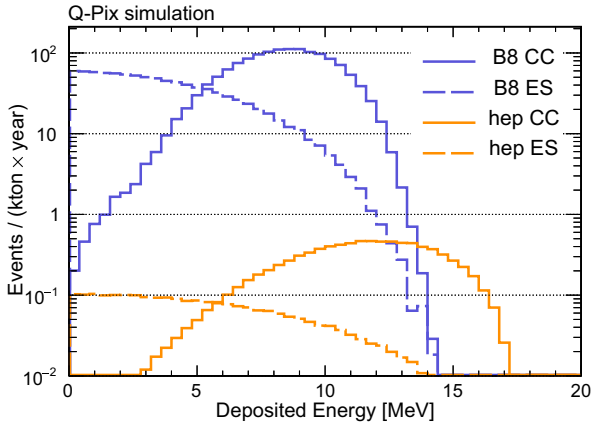

FIG. 2. Energy spectra of the total expected B8 and hep electron neutrinos from CC and ES interactions in a 10 kiloton LAr active volume per year.

interaction. These two specific solar neutrino processes were selected as the B8 process has the highest flux at energies above 2 MeV and the hep process produces the highest neutrino energies. Hep neutrinos have never been observed, but upper limits on their flux have been reported [19,56]. Table I and Fig. 2 show the expected solar neutrino events in a 10 kiloton-year exposure for all four interaction categories (B8CC, B8ES, hepCC, and hepES). These predictions result from the solar neutrino flux from Ref. [57] and the cross section of neutrino interactions in argon [51].

V. BACKGROUND PREDICTIONS

Past solar experiments such as SNO [22] and Borexino [21] have shown that with a good control and understanding of backgrounds, detailed physics analyses can be performed on solar neutrinos.

In this study, we construct a conservative background model representing a generic underground cavern environment. Our approach emphasizes worst-case scenarios by including all potential background sources that could compromise solar neutrino sensitivity below 20 MeV. While the model is not tailored to a specific site, it is designed to capture a full range of rare backgrounds that could impact future measurements. We emphasize that the feasibility of solar neutrino detection is highly dependent on site-specific environmental conditions—including but not limited to rock composition, shielding design, and detector construction. Any experiment-specific implementation is beyond the scope of this work. Finally, we note that dominant backgrounds in the high energy tail (above 11 MeV) are severely underconstrained by current data. A central conclusion of this work is the urgent need for dedicated and site-specific essays to enable robust solar neutrino analyses in future large-scale detectors.

We classify backgrounds in two categories according to their origin. Internal backgrounds are those originating in the fiducial volume of the detector, either from radioactive decays in the liquid argon itself (referred to as "bulk argon radioactivity") or from radioactive isotopes contained in detector components. External backgrounds are those that originate outside of the detector and propagate into the fiducial volume, and are generated from decays in the cavern walls (including the rock concrete and shotcrete) and in the cryostat. External backgrounds are mainly neutrons and γ rays. The mean-free path of α and β particles is too short to reach the liquid argon. The details of the backgrounds considered here are summarized in Table II. Unless it is mentioned otherwise in the following subsections, all backgrounds are simulated using QPixG4.

A. Internal backgrounds

In this section we describe the internal backgrounds that originate in the argon bulk or in the detector components.

1. Argon radioactivity

Commercially available argon commonly used in LArTPCs is obtained by liquefying argon from the atmosphere. In its natural isotopic composition, atmospheric argon consists of the stable ^{40}Ar isotope and trace amounts of the radioactive isotopes ^{37}Ar ($T_{1/2} = 35$ d, $Q_\beta = 0.813$ MeV), ^{39}Ar ($T_{1/2} = 268$ y, $Q_\beta = 0.565$ MeV), and ^{42}Ar ($T_{1/2} = 32.9$ y, $Q_\beta = 0.599$ MeV). Here, $T_{1/2}$ and Q_β refer to the half-life and the energy decay components of the corresponding isotope, respectively. While ^{37}Ar decays via electron capture, ^{39}Ar and ^{42}Ar decay via β emission producing an electron propagating in the detector. If their energy lies between 0.5 and 18.5 MeV, these β electrons can mimic the signature of the solar neutrino events that also produce an electron. We do not consider the decay of ^{37}Ar, since it has a short lifetime (35 days) and we assume that all related activity will be negligible by the time of data taking. Activity of ^{39}Ar and ^{42}Ar in atmospheric LAr has been measured by the WARP [58], GERDA [59], DEAP-600 [60], and DBA [61] experiments to be approximately 1 Bq/kg and 50–100 μBq/kg, respectively. In this study we use 1 Bq/kg for ^{39}Ar, and 100 μBq/kg for ^{42}Ar. We also consider ^{85}Kr ($T_{1/2} = 10.7$ y, $Q_\beta = 0.687$ MeV), which decays via β emission. While the exact ^{85}Kr activity highly depends on the quality of the LAr batch and can vary by up to a factor 3, here we assume an activity of 0.1 Bq/kg [58,62].

The ^{39}Ar and ^{85}Kr daughters are stable. However, ^{42}Ar decays to ^{42}K, which is unstable. ^{42}K β decays to the ground state of ^{42}Ca ($T_{1/2} = 12$ h, $Q_\beta = 3.525$ MeV) with 82% branching ratio, and the remaining 18% to an excited state of ^{42}Ca, emitting an additional 1.524 MeV γ ray. If the ^{42}K daughter remains positively charged, this background chain could potentially be reduced if the $^{42}K^+$ drifts to the cathode before it decays. However, there are no measurements of ion survival probability for $^{42}K^+$ in LAr. Furthermore, at these energies, the enormous background rate would be negligibly impacted by a potential reduction through ion drift. Thus, we make the conservative assumption that the activity of any nucleus daughter is the same as its parent.

The use of underground argon in the low-background scenario significantly reduces internal backgrounds, as discussed in the SLoMo proposal [44]. UAr is significantly more expensive and challenging to obtain than atmospheric argon, but there are large scale experiments such as DarkSide that have already incorporated it into its design [88]. Since UAr is less activated by cosmic-ray interactions, the radioactive isotopes in UAr are suppressed. The assumed ^{39}Ar and ^{85}Kr activities in UAr are 0.73 and 2 mBq/kg, respectively, as measured by DarkSide [63,64]—a reduction of 3 orders of magnitude in both cases. There are no direct measurements of

TABLE II. Summary of all of the background processes considered for the study discussed in Sec. V. All radioactive chains are separated by a solid line and they stop when a stable daughter is reached. The number of expected events for each decay of the chain is computed considering secular equilibrium, where the rate of the daughter is the product of the parent decay rate, its branching ratio, and its decay probability within a one-year time window.

							Expected rate for 10 kt · yr		
Isotope	Half-life (s)	Decay	Q (MeV)	Daughter	BR (%)	Rate (Bq/kg)	High background	Low background	Reference
^{39}Ar	8.5×10^{9}	β	0.565	^{39}K	100	1.1	$\sim 10^{14}$	$\sim 10^{11}$	[44,58–62] [63–65]
^{42}Ar	1.0×10^{9}	β	0.599	^{42}K	100	1.0×10^{-4}	$\sim 10^{10}$	$\sim 10^{7}$	
^{42}K	4.5×10^{4}	β	3.525	^{42}Ca	100	1.0×10^{-4}	$\sim 10^{10}$	$\sim 10^{7}$	
^{85}Kr	3.9×10^{4}	β	0.687	^{85}Rb	100	1.0×10^{-1}	$\sim 10^{13}$	$\sim 10^{10}$	
^{219}Rn	4.0	α	6.946	^{215}Po	100	7.0×10^{-6}	$\sim 10^{9}$	$\sim 10^{6}$	[29,44,66–73]
^{215}Po	1.8×10^{-3}	α	7.526	^{211}Pb	99.99977	7.0×10^{-6}	$\sim 10^{9}$	$\sim 10^{6}$	
^{215}Po	1.8×10^{-3}	β	0.721	^{215}At	0.00023	1.6×10^{-11}	$\sim 10^{3}$	$\sim 10^{0}$	
^{211}Pb	0.6	β	1.367	^{211}Bi	100	7.0×10^{-6}	$\sim 10^{9}$	$\sim 10^{6}$	
^{215}At	1×10^{-4}	α	8.178	^{211}Bi	100	1.6×10^{-11}	$\sim 10^{3}$	$\sim 10^{0}$	
^{211}Bi	3.6×10^{-2}	α	6.750	^{207}Tl	99.72	7.0×10^{-6}	$\sim 10^{9}$	$\sim 10^{6}$	
^{211}Bi	3.6×10^{-2}	β	0.574	^{211}Po	0.28	2.0×10^{-8}	$\sim 10^{6}$	$\sim 10^{3}$	
^{207}Tl	7.9×10^{-2}	β	1.418	^{207}Pb	100	7.0×10^{-6}	$\sim 10^{9}$	$\sim 10^{6}$	
^{211}Po	0.5	α	7.594	^{207}Pb	100	2.0×10^{-8}	$\sim 10^{6}$	$\sim 10^{3}$	
^{220}Rn	55.6	α	6.404	^{216}Po	100	5×10^{-3}	$\sim 10^{12}$	$\sim 10^{9}$	
^{216}Po	0.1	α	6.906	^{212}Pb	100	5×10^{-3}	$\sim 10^{12}$	$\sim 10^{9}$	
^{212}Pb	3.8×10^{4}	β	0.569	^{212}Bi	100	5×10^{-3}	$\sim 10^{12}$	$\sim 10^{9}$	
^{212}Bi	3.6×10^{3}	β	2.251	^{212}Po	64	3.2×10^{-3}	$\sim 10^{12}$	$\sim 10^{9}$	
^{212}Bi	3.6×10^{3}	α	6.207	^{208}Tl	36	1.8×10^{-3}	$\sim 10^{11}$	$\sim 10^{8}$	
^{208}Tl	1.8×10^{2}	β	4.999	^{208}Pb	100	3.2×10^{-3}	$\sim 10^{11}$	$\sim 10^{8}$	
^{212}Po	3.0×10^{-7}	α	8.954	^{208}Pb	100	1.8×10^{-3}	$\sim 10^{12}$	$\sim 10^{9}$	
^{222}Rn	3.3×10^{5}	α	5.590	^{218}Po	100	1.0×10^{-3}	$\sim 10^{11}$	$\sim 10^{8}$	
^{218}Po	1.9×10^{2}	α	6.114	^{214}Pb	99.98	1.0×10^{-3}	$\sim 10^{11}$	$\sim 10^{8}$	
^{218}Po	1.9×10^{2}	β	0.259	^{218}At	0.02	2.0×10^{-7}	$\sim 10^{7}$	$\sim 10^{4}$	
^{214}Pb	1.6×10^{3}	β	1.018	^{214}Bi	100	1.0×10^{-3}	$\sim 10^{11}$	$\sim 10^{8}$	
^{218}At	1.3	α	6.874	^{214}Bi	99.9	2.0×10^{-7}	$\sim 10^{7}$	$\sim 10^{4}$	
^{218}At	1.3	β	2.881	^{218}Rn	0.1	2.0×10^{-10}	$\sim 10^{4}$	$\sim 10^{1}$	
^{218}Rn	2.1×10^{3}	α	7.262	^{214}Po	100	2.0×10^{-10}	$\sim 10^{4}$	$\sim 10^{1}$	
^{214}Bi	1.2×10^{3}	β	3.269	^{214}Po	99.97	1.0×10^{-3}	$\sim 10^{11}$	$\sim 10^{8}$	
^{214}Bi	1.2×10^{3}	α	5.621	^{210}Tl	0.021	2.1×10^{-7}	$\sim 10^{7}$	$\sim 10^{4}$	
^{214}Bi	1.2×10^{3}	α/β	3.270	^{210}Pb	0.003	3.0×10^{-8}	$\sim 10^{6}$	$\sim 10^{3}$	
^{214}Po	1.6×10^{-4}	α	7.883	^{210}Pb	100	1.0×10^{-3}	$\sim 10^{11}$	$\sim 10^{8}$	
^{210}Tl	78.0	β	5.483	^{210}Pb	99.991	2.1×10^{-7}	$\sim 10^{7}$	$\sim 10^{4}$	
^{210}Tl	78.0	β/n	0.294	^{209}Pb	0.009	1.9×10^{-11}	$\sim 10^{3}$	$\sim 10^{0}$	
^{209}Pb	1.2×10^{4}	β	0.644	^{209}Bi	100	1.9×10^{-11}	$\sim 10^{3}$	$\sim 10^{0}$	
^{209}Bi	6.3×10^{26}	α	3.137	^{205}Tl	100	0.0	$\sim 10^{0}$	$\sim 10^{0}$	
^{210}Pb	7.0×10^{8}	β	0.063	^{210}Bi	99.999998	3.1×10^{-5}	$\sim 10^{9}$	$\sim 10^{6}$	
^{210}Pb	7.0×10^{8}	α	3.792	^{206}Hg	0.000002	5.8×10^{-13}	$\sim 10^{2}$	$\sim 10^{-1}$	
^{206}Hg	4.9×10^{2}	β	1.308	^{206}Tl	100	5.8×10^{-13}	$\sim 10^{2}$	$\sim 10^{-1}$	
^{210}Bi	4.3×10^{5}	α	5.036	^{206}Tl	0.0001	3.1×10^{-11}	$\sim 10^{3}$	$\sim 10^{0}$	
^{210}Bi	4.3×10^{5}	β	1.162	^{210}Po	99.9999	3.1×10^{-5}	$\sim 10^{9}$	$\sim 10^{6}$	
^{206}Tl	2.5×10^{2}	β	1.532	^{206}Pb	100	5.8×10^{-13}	$\sim 10^{2}$	$\sim 10^{-1}$	
^{210}Po	1.2×10^{7}	α	5.407	^{206}Pb	100	2.6×10^{-5}	$\sim 10^{9}$	$\sim 10^{6}$	
α capture							$\sim 10^{6}$	$\sim 10^{3}$	[74,75]
n inelastic							$\sim 10^{6}$	$\sim 10^{2}$	[29,44,76]
n capture							$\sim 10^{7}$	$\sim 10^{3}$	[77–82]
Cavern γ							$\sim 10^{11}$	$\sim 10^{11}$	[23,83–87]

^{42}Ar activity in UAr, and even though its activity is expected to be reduced more significantly than that of ^{39}Ar and ^{85}Kr [44,65], we assume a reduction of 3 orders of magnitude for the low-background scenario in line with the other two isotopes [44,65].

2. Radon decay chains

Radon emanates from any material that contains uranium and thorium isotopes, such as detector components and surrounding materials like rocks, concrete, and shotcrete, and can diffuse inside the detector. Here, we treat radon isotopes and their daughters as an internal background since their activity will primarily occur inside the detector. In line with Ref. [44], we assume an activity of 1 mBq/kg for ^{222}Rn originating from the ^{238}U chain. Since the measured ^{238}Th abundance is 1.5 to 5 times higher than ^{238}U [29,66–68] and ^{220}Rn is a daughter of ^{238}Th, we assume a conservative ^{220}Rn activity of 5 mBq/kg, 5 times larger than ^{222}Rn. Finally, for ^{219}Rn, which originates from ^{235}U, we estimate an activity of 7μ Bq/kg [69] based on the relative abundance of uranium isotopes. Each of the above radon isotopes generates a radioactive decay chain that includes α and β decays with different energies. The decays used in this study are presented in Table II. The number of expected events for each decay of the chain is computed considering secular equilibrium, where the rate of the daughter is the parent decay rate multiplied by its branching ratio and by its decay probability in a one-year time window. For long-lived isotopes, such as ^{210}Pb, an accumulation and thus an activity increase is expected over time. However, as will be seen later, the results presented here are independent of these particular decays and any subsequent decay.

As previously mentioned, β emitters and solar neutrinos both generate one primary electron propagating in the detector. Even though most of the background β electrons have a maximum energy below 2–3 MeV, thallium isotopes ^{208}Tl and ^{210}Tl have a higher Q_β of 5 and 5.4 MeV, respectively. The electrons can carry up to 2.38 MeV for ^{208}Tl decays, with the remaining energy emitted as γ rays, and up to 4.4 MeV for ^{210}Tl decays. We estimate $\sim 10^7$ ^{210}Tl decays per 10 kton-year exposure, which is 2 orders of magnitude more than the total number of expected solar neutrino events with energies < 4.4 MeV, making this a significant source of background.

While ionizing α particles from α emitters can be discriminated from solar neutrinos via their different ionization profiles, α particles can be captured by ^{36}Ar, ^{38}Ar, and ^{40}Ar in "giant resonances" that deexcite and emit γ rays with energies between 1 and 17 MeV [74]. These γ rays are an important background for solar neutrino detection, since—just like solar neutrinos—they can produce electrons in the active volume by Compton scattering or pair production. The α-capture processes are not yet measured with good precision (currently there is a 30% uncertainty on cross-section measurements [74]). Nevertheless, we attempt to estimate the rates of this additional γ background, given its potential impact on the study of solar neutrinos. The α-capture differential cross section in argon is reported in [74] for α energies between 5.5 and 15 MeV, at 90° with respect to the beam direction. They are also reported to happen down to 3 MeV of α energies in [89]. Starting from those values and considering the isotropy of our use case, we calculate the interaction probability for the different α energies under the assumption of continuous slowing down approximation down to 3 MeV, integrating over the full solid angle. We obtain an α-capture rate of almost $\sim 10^4$ per 10 kiloton per year. We also simulate this process in QPixG4 by generating α particles isotropically inside the detector with the energies and relative frequencies presented in Table II, obtaining a rate of $\sim 10^6$ α captures per 10 kiloton per year, which seems to overestimate the measurements presented in Ref. [74]. The obtained γ spectrum is presented in Fig. 3. Given the profound impact of α-capture backgrounds on the study of solar neutrinos, the large uncertainties on the measured process [74], and the potential inaccuracy of simulations relying on minimal data available, we conservatively assume the rate predicted by Geant4 with the caveat that new measurements of α capture are of paramount importance to draw any final conclusion on the observability of hep neutrinos and the study of solar neutrinos in general.

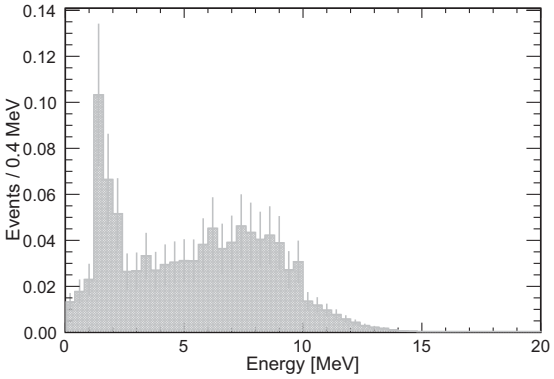

FIG. 3. Simulated energy spectrum of the γ rays produced in α-capture processes in argon. The error bars represent the uncertainty on the cross-section measurement. The spectrum is normalized to 1.

α particles can also interact with argon nuclei via $^{40}\mathrm{Ar}(\alpha, \mathrm{n}\gamma)^{43}\mathrm{Ca}$ [90], emitting neutrons and γ rays in the final state. Based on the simulation, we expect $\sim 10^7$ of these reactions per year. The simulation of this process shows that the γ has an energy range of [0.3,6.2] MeV, similar to what is reported in Ref. [75], while neutron energy can reach 3.6 MeV. As these energies are below the energies of external neutrons and γ rays presented in the following sections, and their rate is significantly lower, we neglect their contributions.

In addition to the α particles produced by radon decay chains, one Rn daughter, ^{210}Tl, can also undergo β-delayed neutron emission. Whenever the β decay populates excited states in the daughter nucleus above the neutron separation energy, neutron emission becomes energetically allowed. This neutron carries the excess energy of 5.189 MeV. As in the previous case, the rate of this particular decay is very low compared to that of external neutrons, and we therefore do not include it in our background model.

The summary of all of the decays coming from radon isotopes, with their respective activities and half-lives, is presented in Table II. As previously mentioned, some nuclei resulting from radioactive decays may remain positively charged, thus drifting towards the cathode and potentially being removed if their half-lives are larger than the drift time. EXO-200 [70] reports the ion survival probability of ^{218}Po$^+$ (result of an α decay) and ^{214}Bi$^+$ (result of a β decay) in liquid xenon to be approximately 50% and 75%, respectively, and DarkSide [71] reports the ion survival probability of ^{218}Po$^+$ in LAr to be 37%—significantly lower than in LXe. The survival probability ultimately depends on the recombination effect, which depends on the electric field applied in the active volume, but it also depends on the LAr purity (as ions can recombine with electrons from impurities) and LAr flow dynamics, as ion drift velocity is of the same order of magnitude as LAr flow velocity. While this effect could reduce backgrounds, we conservatively assume that the activity of any nucleus daughter is the same as its parent given that the potential reduction is small compared to the difference in expected signal and background. For example, it takes four decays to produce ^{208}Tl (^{220}Rn $\rightarrow$ ^{216}Po $\rightarrow$ ^{212}Pb $\rightarrow$ ^{212}Bi $\rightarrow$ ^{208}Tl). Assuming a 50% ion survival probability, and assuming that all surviving ions are collected before decaying, the ^{208}Tl rate would be reduced from 10^{12} to $\sim 10^{10}$, still 5 orders of magnitude more than the number of expected solar neutrino events.

In the low-background scenario, the use of a dedicated radon purification system combined with careful fabrication and installation procedures can reduce the radon activity in the detector by 3 orders of magnitude [44]. Such reduction has already been demonstrated in dark matter experiments such as DarkSide, with a radon concentration of 2 μBq/kg [72], and even improved by DEAP-600 [73], with a concentration of 0.2 μBq/kg. Therefore, when considering the low-background scenario, we reduce all decays associated with Rn activity by 3 orders of magnitude.

3. Radioactivity from detector components

The last sources of internal background we consider are the detector components. The different detector parts contain radiocontaminants such as ^{238}U, ^{235}U, ^{238}Th, ^{60}Co, or ^{40}K that can produce background events. However, since it is expected that the support structures needed for a Q-Pix readout will be simple and lightweight, we neglect the potential radioactive decays from the detector components. Finally, while ^{238}U, ^{235}U, and ^{238}Th lead to the aforementioned radon chains, ^{60}Co and ^{40}K are low-energy β emitters (< 1.5 MeV) that do not affect the conclusions presented at the end of this study.

B. External backgrounds

In this section we describe the backgrounds that originate outside the cryostat.

1. Neutrons

Neutrons are emitted in fission processes and (α, n) reactions created by α decays resulting from the ^{238}Th and ^{238}U chains. To estimate the neutron energy spectrum from the cavern, we use the material compositions in Ref. [29]. The (α, n) components of the neutron spectrum used in this study are generated via the NeuCBOT [76] software. The uranium spontaneous fission component of the neutron spectrum is calculated using the Watt spectrum, with a neutron yield of two neutrons per decay, similar to Ref. [29]. The neutron flux in the cavern is assumed to be 1×10^{-5} n/cm^2/s, in line with Ref. [44], which corresponds to neutrons penetrating the LAr surface with a frequency of 12 Hz. This assumption is consistent with the values reported by SK [23] and in the YangYang cavern [91], and 1 order of magnitude above the flux measured in Gran Sasso [83]. The total simulated neutron energy spectrum is shown in Fig. 4. Neutrons are then propagated in LAr using the QPixG4 package.

In argon, neutrons with energy above 1.46 MeV can undergo inelastic scattering [77,78]. This can generate γ cascades with energies reported in the range of [1.46, 11.77] MeV [77]; however, the γ rates decrease rapidly with energy. These γ rays are an important background, as they can generate electrons by Compton scattering or pair production mimicking solar neutrino signals. Combining the measured neutron-argon inelastic cross section [78], the assumed neutron flux, and our QPixG4 simulation, we estimate a neutron inelastic scattering frequency of 0.2 Hz per 10 kiloton.

Below 1.46 MeV, neutrons undergo elastic scattering with high rates in the keV energy region until they thermalize. Since this is far below our energy range of interest in the MeV, we neglect this contribution. Finally, thermal neutrons can be captured by argon nuclei. Neutron captures on ^{40}Ar and ^{36}Ar generate γ cascades up to 6.1 and 8.8 MeV, respectively [79,80]. Neutron captures on impurities as ^{14}N can reach higher energies [81], but given the expected purity levels of LAr [92], we consider these contributions negligible. The rate of neutron captures in the active volume of the detector is found to be 1 Hz per 10 kton. To correctly simulate the γ cascades, we

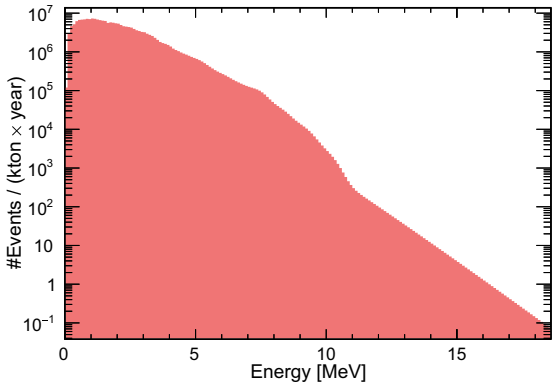

FIG. 4. Energy spectrum for the simulated neutrons produced in the cavern walls and reaching the liquid-argon surface.

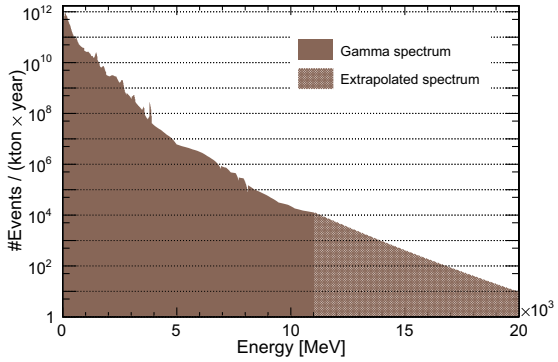

FIG. 5. True energy spectrum of the external γ rays incident on the LAr interfaces based on measurements performed in underground facilities around the world [23,83–87]. The cross-hatched tail corresponds to the exponential extrapolation.

reweighted the QPixG4 output for the γ cascade process to match the measured data in Ref. [82].

In the low-background scenario, we assume the use of water shield of 50 cm in combination with a borated cryostat to reduce the neutron flux reaching the active volume of the detector. Water has been used as a passive shield in numerous low-energy experiments such as LZ [93], XENON1nT [94], DEAP-3600 [95], PandaX [96], Borexino [15], and GERDA [97], where several meters of water reduce the impact of radiogenic neutrons to negligible [98,99]. Simulations have shown that 50 cm of water, the installation of which could be accomplished with the use of water bricks, can reduce the neutron flux in our range of interest between 3 and 4 orders of magnitude [29,100], and therefore we reduce the simulated neutron rates shown in Fig. 4 by 10^4 for the low-background scenario.

2. γ rays

The interactions of γ rays in the liquid argon are an irreducible background as they result in the production of single electrons via Compton scattering or pair production. It is therefore crucial to estimate the rates of γ rays produced in the detector surroundings, referred to here as "external γ rays." The γ rays from radioactive decays can reach energies of approximately 3 MeV. Neutrons produced from fission or (α, n) reactions can be captured in the cavern, in the concrete or shotcrete of the cavern walls, and in the cryostat, generating more energetic γ rays, with energies up to 11.5 MeV [101]. Finally, α particles generated in the aforementioned radioactive chains and fission reactions can interact or be captured by nuclei in the cavern and the shotcrete, generating even more energetic γ rays. For example, α captures in magnesium and silicon lead to deexcitation energies of more than 17 MeV [102]. The effects of γ rays are minimally mitigated by the cryostat material and they are expected to propagate of the order of 10–100 cm in liquid argon.

To quantify the impact of external γ rays on our conclusions, we perform a detailed review of γ-ray rates as measured in existing experiments to validate simulations. Even though the composition of the cavern rocks and building materials (e.g., shotcrete) affects the exact γ flux of all underground laboratories, the observed similarities in the relative frequencies of the γ-ray energies build confidence in the spectrum considered in this work. As our starting point, we use the γ-ray spectrum measured up to 3 MeV by the LZ Collaboration in the Davis cavern [84]. They report a total γ-ray flux of 1.9 $\gamma/\mathrm{cm}^2/\mathrm{s}$, which we take as normalization. This value is similar to the one reported by SK [23] and slightly above those reported in Gran Sasso [83] and the SNO cavity [85], and implies that γ rays enter the liquid-argon surface with a rate of 4 MHz. To expand this spectrum to higher γ energies, we leverage the measurements performed in other underground facilities such as Gran Sasso [83], SNOLAB [85], YangYang [86], Jinping [87], and Kamiokande [23]. We generate a weighted average spectrum that is added to the one reported by the LZ Collaboration. This new spectrum reaches to energies of $\approx$11 MeV, consistent with the γ rays result of neutron captures. As discussed previously, physical processes can occur in the cavern that generate even more energetic photons. To account for these, which are subdominant to those originated from neutron interactions, we arbitrarily choose to extrapolate the averaged spectrum up to 20 MeV exponentially. This choice, although very conservative, is used to account for the potential background events observed in the high energy region of the solar neutrino spectrum by other experiments [19,24]. The resulting spectrum is presented in Fig. 5. In the spectra reported in underground facilities around the world, the fraction of γ rays above 5 MeV covers a wide range of $10^{-8} - 10^{-5}$. This variability in the estimate of the high energy component is relevant as high rates of γ backgrounds above 5 MeV can dominate in the solar neutrino signal region for B8 and hep neutrinos. Hence, dedicated

measurements of the external γ spectrum, especially at energies above 5 MeV, will be crucial to estimate sensitivities to solar neutrinos.

External γ background is not considered in the SLoMo proposal [44]. We therefore do not assume further reduction strategies for the γ background in our low-background scenario and use the predicted rates discussed in this section.

VI. RESULTS

In this section, we present the results obtained from our simulations of solar neutrinos and backgrounds using the assumptions described in Secs. IV and V. We investigate several potential background reduction strategies and we report the data rates expected in the Q-Pix data acquisition that would allow for a continuous readout, essential to study solar neutrinos.

Figure 6 (top) shows the spectra of deposited energy for all the backgrounds considered (see Sec. V) in the high-background scenario. Even in the low-background scenario, the spectrum of solar neutrinos is at least 3 orders of magnitude lower than the background when no background rejection strategy is applied. Studying solar neutrinos below 8 MeV is virtually impossible, as the background rates from radioactive decays, which are the ones predicted with the highest confidence in this study, are between 8 and 11 orders of magnitude above the solar neutrino signal. Above an energy of 8 MeV, the γ-ray backgrounds (both from external γ rays and from α captures) are the dominant ones. In the 8–12 MeV window, the detection of solar neutrinos appears possible, but will strongly rely on experimentally constraining the background precisely.

Figure 6 (bottom) shows the same deposited energy spectra for the low-background detector scenario. While many backgrounds are significantly reduced, the cavern γ rays (which are not reduced in this scenario) and the γ rays resulting from α capture remain the main challenge—highlighting the importance of *in situ* measurements of these backgrounds.

In the next section, we investigate the potential to reduce these backgrounds at the reconstruction level (Sec. VI A) and with additional tools such as fiducialization (Sec. VI B), directionality (Sec. VI C), or light detection (Sec. VI D).

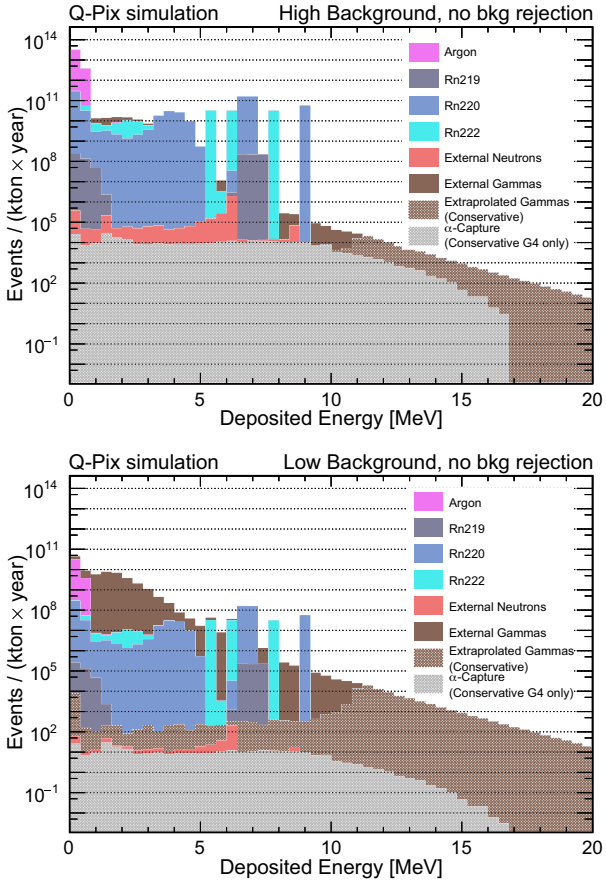

FIG. 6. Energy spectra of all signal and background sources for the high-background scenario (top) and low-background scenario (bottom) before any selection tool has been applied.

A. Background rejection with Q-Pix clustering

The first step to discriminate signal and background events is to use the clustering tools described in Sec. III, since different particle types may have specific topological signatures and energies. Only α interactions present significant topological differences, whereas β, γ (via Compton scattering or pair production), and neutron interactions (via capture or inelastic scattering, producing γ rays) all result in the production of single electrons that have identical topology to solar neutrino interactions. Neutrons and γ rays can leave additional "blips" (isolated energy depositions) in the event that could be used to veto. Given the very high event rates of all of the other backgrounds, the topological identification of multiple blips for neutron and γ rejection grants in detail consideration and is beyond the scope of this paper. We investigated the impact of the clustering threshold (CT) on background suppression.

The α particles, which will have a short very small range in LAr, will leave a very different signature compared to that of single electrons. In our study, we found that α particles get clustered with a maximum of four resets, which is equivalent to the number of resets that a ~1 MeV electron would deposit in our readout. It is also possible to further use this reset threshold to remove areas of the event spectrum shown in Fig. 6 where the signal is completely buried under background, which is around 3 MeV. For the remaining of the paper, we apply a reset threshold cut of 12, which corresponds to an equivalent deposited energy of 3 MeV, removing all events below this energy. This value sets the energy threshold for the detection of solar neutrinos of this study.

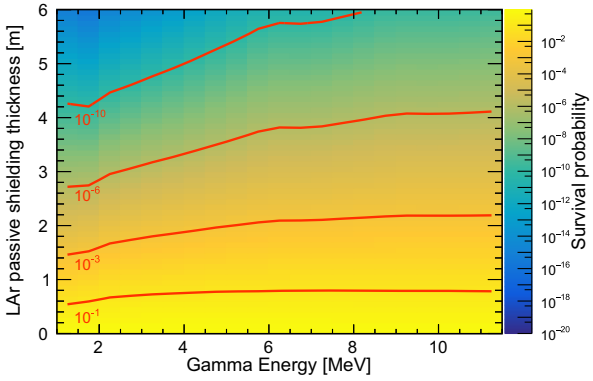

FIG. 7. External γ survival probability as a function of initial energy and the thickness of argon used as passive shielding. The 10^{-1}, 10^{-3}, 10^{-6}, and 10^{-10} contours are shown in red.

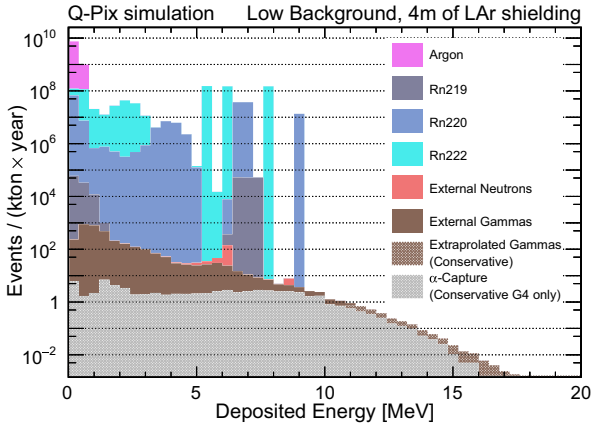

FIG. 8. Deposited energy spectrum of signal and background sources for the low-background scenario using 4 m of LAr as passive shielding.

B. Fiducialization

Since one of the major backgrounds consists of radiation produced outside the detector, we explore the obvious option of fiducializing the argon volume to reduce the impact of cavern γ rays and neutron inelastic scattering. Figure 7 shows the external γ survival probability as a function of the initial γ energy and the distance from the cryostat walls. As expected, γ events are suppressed exponentially as a function of the fiducializing distance, while the isotropic nature of the solar neutrino interactions makes the reduction in signal only linear.

We provide here an example of the use of the fiducialization tool alone. By considering the straightforward (but aggressive) strategy of using 4 m of argon as passive shielding, the active volume is reduced to the two innermost TPC volumes (see Fig. 1) of which only 6 m of height and 54 m of length remain usable (here we consider 0.5, 1, and 1.9 m of clearances between the detector and the cryostat in the drift, vertical and horizontal axis). This allows the retention of about 20% of the total argon active mass (≈2.3 kt). The event rejection on the vertical and longitudinal axis can be accomplished precisely by Q-Pix, as the pixels' 4 mm pitch provides enough spatial resolution for this task. This fiducialization scheme results in the retention of $\sim\mathcal{O}(10^4)$ solar neutrino events, $\sim\mathcal{O}(10^4)$ γ rays, and $\mathcal{O}(1)$ neutron inelastic scattering events per year. As can be seen in Fig. 8, the stringent fiducialization allows to see much more of the solar neutrino signal over a larger range of energies. The hep signal also becomes visible. However, the capability to observe the hep neutrinos will depend on the detailed understanding of the γ rays from the α capture on argon and of the external γ rays above 11 MeV. It will also require a sufficient energy resolution in order to identify the hep signal in the ∼15–18 MeV range. These simple fiducialization strategy can be used as guidance for any study of solar neutrinos, but specific optimizations will be necessary in any dedicated analyses where multiple background rejection strategies are applied in conjunction, and are thus beyond the scope of this paper.

C. Background rejection with directionality

One key difference between solar neutrino interactions and backgrounds is that neutrinos originate from a known direction: the Sun. While neutrino CC interactions do not retain any directional information from the incoming neutrino, ES events do. A previous study of the detectability of neutrinos from supernovae [53] showed that Q-Pix enables the reconstruction of the direction of electrons from low-energy ES neutrino interactions. Thus, we explore the possibility of using directionality as a background discrimination tool in the case of solar neutrinos.

In this study, we assume that the Q-Pix clustering threshold is set to 12 resets, enough to suppress all events depositing less than 3 MeV of energy. We reconstruct the directionality of the primary electrons from ES events following the procedure in our previous supernova study with Q-Pix [53]. We define θ as the angle between the true neutrino direction from the simulation and the reconstructed electron direction. In our study, signal events are generated following the reconstructed angular distribution of the ES reaction, later converted to the $\cos\theta$ space. At first approximation, background events follow an isotropic distribution in $\cos\theta$. The angular distributions of signal (ES) events and uniform background events are presented in Fig. 9. We study the signal sensitivity via a likelihood ratio test. The signal and background joint distribution is fitted under the $\mathcal{H}_0$ (only background) and the $\mathcal{H}_1$ (signal plus background) hypothesis, from which h_0 and h_1 likelihoods are respectively obtained. The statistic $-2\ln(h_0/h_1)$ of the joint distribution is then compared to that of the background-only distribution and the median sensitivity to the signal is extracted.

While in the case of supernova neutrinos directionality was proved to be a powerful tool to point back to the

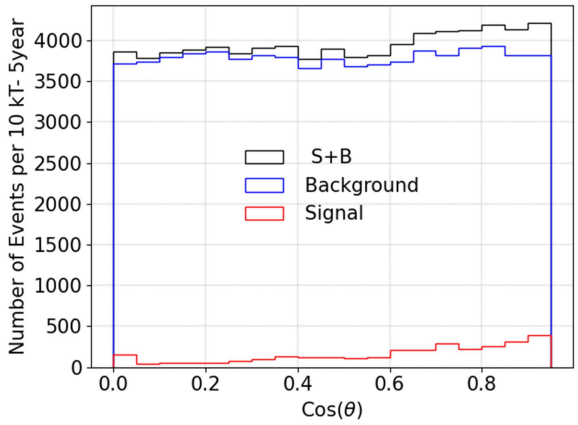

FIG. 9. Signal (red), background (blue), and total event (black) histograms for the events with reconstructed energy between 6 and 12 MeV in 10 kT for a period of five years. θ is the angle between the direction of the sun and the reconstructed primary electron's direction. The low-background scenario and a 4 m fiducialization strategy are assumed here.

supernova event, we find that its discrimination power in the case of solar neutrinos is severely hampered by the high level of backgrounds. If we combine directionality and a stringent fiducialization (4 m) in the low-background scenario, we find that we can expand sensitivity to solar neutrinos in the 6 to 12 MeV region. Without fiducialization or in our high-background scenario, the high level of backgrounds completely disallows the identification of the solar neutrino population on the directionality plot.

D. Background rejection with light detection

Light detection in a LArTPC provides additional event information, such as timing, position, and energy sensitivity. In this section, we identify areas and tools where a powerful light collection system can confer additional benefits compared to the measurement of charge alone.

The results are obtained via a Geant4 toy simulation of the full detector geometry where the light production and propagation are simulated in full, but no photosensitive element is explicitly defined. Instead, we assume a photon detection system that provides 100% light coverage at the pixel planes, in line with a proposed innovative solution for a dual charge-light readout using Q-Pix [46], and corresponding to 37% light coverage for the full detector. We assume a conservative 15% photon detection efficiency, similar to current performances of commercial photosensors [45], and a timing resolution better than 10 ns. From these assumptions we estimate the associated background rejection factor.

We highlight two specific techniques leveraging light detection, namely pulse-shape discrimination between signal and background γ rays from α-capture events, and delayed light emission from the excited $^{40}K^{*}$ produced in CC interactions:

$$\nu_e + {}^{40}\mathrm{Ar} \rightarrow {}^{40}\mathrm{K}^{*} + e^{-}. \quad (1)$$

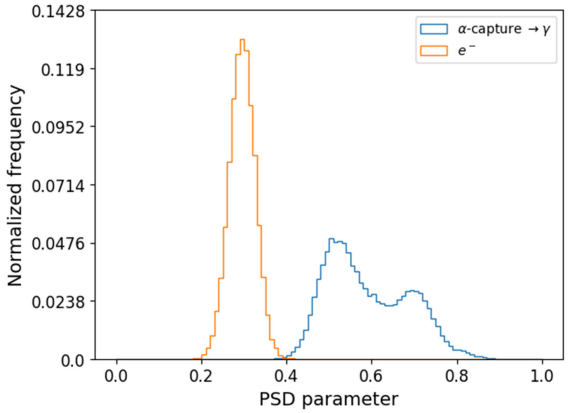

FIG. 10. Distribution of the ratio of fast and slow scintillation light (PSD parameter) for electrons (orange) and α-capture γ rays (blue).

1. Pulse-shape discrimination

Figure 6 highlights the background contributions from the poorly constrained α-capture process reaching up to 17 MeV in energy and thus interfering with the major portions of ^{8}B and hep solar neutrino spectra.

The γ rays produced by ionizing α particles capturing on argon present a different scintillation light profile compared to electrons or regular γ rays in LAr. When the α particle ionizes the medium before being captured, the initial ionization by the α skews the scintillation distribution for α captures [103], allowing to use pulse-shape discrimination (PSD) techniques to differentiate α-capture γ events from solar neutrino events. By comparing the ratio of fast and slow scintillation light, rejection of α-capture events is achievable. Figure 10 shows the distribution of the PSD parameter for both signal (electrons) and background (γ rays from α capture) events. This parameter represents the ratio between the fast and slow component of the light, where the integration window for the fast component is set at 50 ns.

By selecting events with a PSD < 0.4, the study shows that 99% of electron events can be retained while rejecting 99% of events from α-capture events where the α ionizes. While this result is encouraging, our study uncovered limitations in the simulation of the α transport in the range from 1.1 to 8.9 MeV in Geant4. In particular, we find that Geant4 reports zero ionization for more than 60% of α-capture events. To understand the exact amount of ionization produced by α particles before they capture as a function of energy, a dedicated measurement of α-capture processes in liquid argon will be needed to draw solid conclusions about this harmful background.

2. Light coincidence from solar neutrino CC interactions

Charge current interactions from solar neutrinos on argon (1) could be isolated from background via the

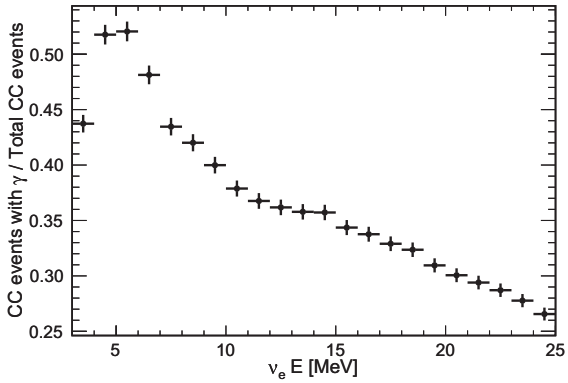

FIG. 11. Fraction of CC events generating a delayed γ as a function of the energy of the incoming solar neutrino.

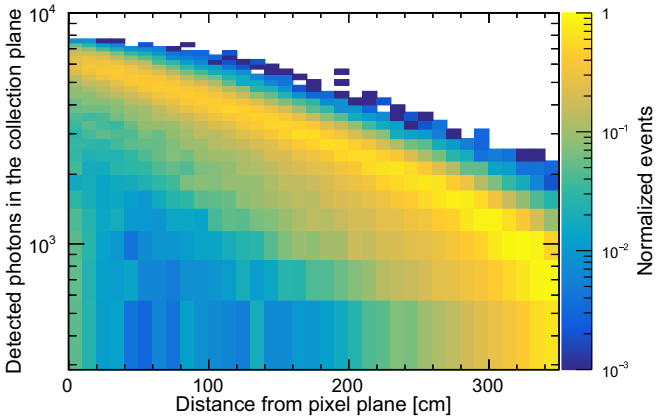

FIG. 12. Photon yield for the delayed γ as a function of the distance to the pixel plane.

detection of a delayed light flash emitted by the deexcitation of the $^{40}K^{*}$ [104]. Figure 11 shows the fraction of CC interactions for which the final-state $^{40}K^{*}$ atom can deexcite by emitting a 1.64 MeV γ with half-life of 336 ns [77]. While 336 ns is too short a time to produce distinguishable charge signals, it is long enough to resolve via light detection.

Figure 12 shows the number of detected photons arriving at our assumed light detection system placed on the anode plane for 1.64 MeV γ rays isotropically distributed inside the detector. Even for delayed flashes emitted 3.5 meters away from the anode, which is the drift distance in our detector geometry, the number of photons detected is of the order of thousands, building confidence in the feasibility of this technique. We define a time window of 1500 ns to determine a signal coincidence, since such time frame contains more than 99% of the delayed γ flashes.

Given the enormous rate of background events, and under the assumption that all background events will produce scintillation light, the viability of this tool depends on the expected number of false positives produced by random background coincidences. For every background

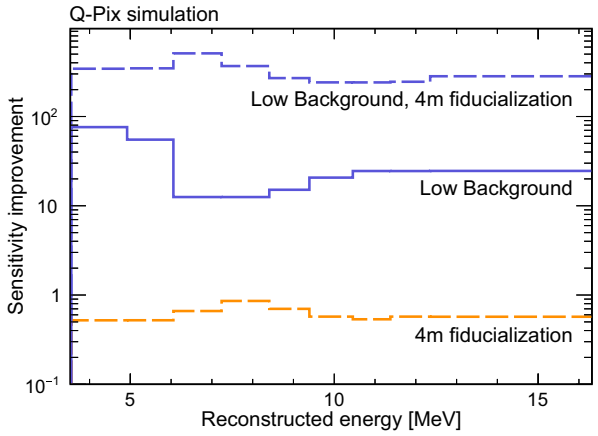

FIG. 13. Improvement of background rejection for a solar neutrino measurement in different detector scenarios with respect to the high-background case when utilizing the delayed-flash technique and the strong fiducialization. The improvements are calculated as the ratios of the $s/\sqrt{b}$ values.

source considered in Table II, the expected number of events $\mu_{bkg,i}$ in a time window of 1500 ns is computed. $P(\mu_{bkg,i}, 0) = e^{-\mu_{bkg,i}}$ represents the Poissonian probability of zero events happening in that time window. The probability of zero random background coincidences after an initial event is computed as the product of the individual probabilities, $P(0) = \prod_i P(\mu_{bkg,i}, 0)$. Here, we consider all different sources of signal and background to be independent, and we neglect contributions between different drift volumes. Under our high-background scenario and considering the full 10 kton active mass, the probability of a random coincidence is approximately 99%. However, in the low-background scenario, the probability of a random coincidence is only 33%. Further considering 4 m of liquid argon used as passive shielding, the random coincidence probability drops to 87% and 0.1%, respectively, for the high-background and low-background scenarios. Following the same strategy that was presented in the directionality studies, the Q-Pix clustering algorithm can be used as a preselection tool. We set a clustering threshold of 12 resets to select events with energy higher than 3 MeV, allowing the light detection system to be used afterwards to identify a potential delayed γ pulse. The number of signal events is computed as the number of CC events passing the CT cut, multiplied by the fraction of events generating a delayed γ. The background coincidences are computed as events passing the CT cut (namely, background electrons with energy above ~3 MeV) followed by a light flash produced by any other event. Figure 13 shows the sensitivity improvement to solar neutrinos (hep and ^{8}B CC channels) when utilizing the fiducialization and the coincidence technique for the different detector scenarios. One can see that applying the fiducialization strategy does not work in the high-background scenario, as the background coincidences

mimicking the delayed flash are dominated by internal backgrounds. However, when both of these tools are applied in the case of the low-background, fiducialized scenario, sensitivity to solar neutrinos is boosted by more than a factor 100 from 3.5 MeV to the higher end of the solar neutrino spectrum in terms of reconstructed energy, despite the rather low total number of solar neutrino events per year.

E. Expected data rates

Figure 14 shows the expected Q-Pix data rates estimated for the solar neutrino events and the leading background sources for the high-background and the low-background scenarios after a preselection of a minimum of 12 resets (∼3 MeV) per event. Data rates in Q-Pix are calculated by counting the number of resets in the events and considering that each reset occupies 8 bytes of memory. The total data rate to store all energy depositions above 3 MeV, needed for an off-line solar neutrino analysis, is estimated to be ∼1 TB per year. If recording data below 3 MeV is desired, Q-Pix can store all events with a minimum of one reset (i.e., events with deposited energy $\gtrsim$0.15 MeV), leading to a total data rate of ∼1 PB per year, still a manageable amount.

In comparison, the expected data size for an event readout from a wire or CRP-based LArTPC is much larger. Reading out a full wire-based 10-kton DUNE module occupies about 6.5 GB if waveforms are recorded for 5.4 ms [105] and 8 GB if data from a CRP readout is recorded for 4.25 ms [39]. We estimate that the rate of events worth recording for a solar analysis—signals and backgrounds that deposit 3 MeV or more—is around 300 Hz. Such a high rate implies that at least one potential solar event is present in each drift time of a wire- or CRP-based detector. Continuously reading out such detectors for a year would generate of the order of 10^5 PB of data. If advanced trigger techniques can allow to record information of a single APA or CRP instead of the full detector, the data rate could be reduced by 2 orders of magnitude—still significantly higher than the expected rates generated by the Q-Pix continuous readout.

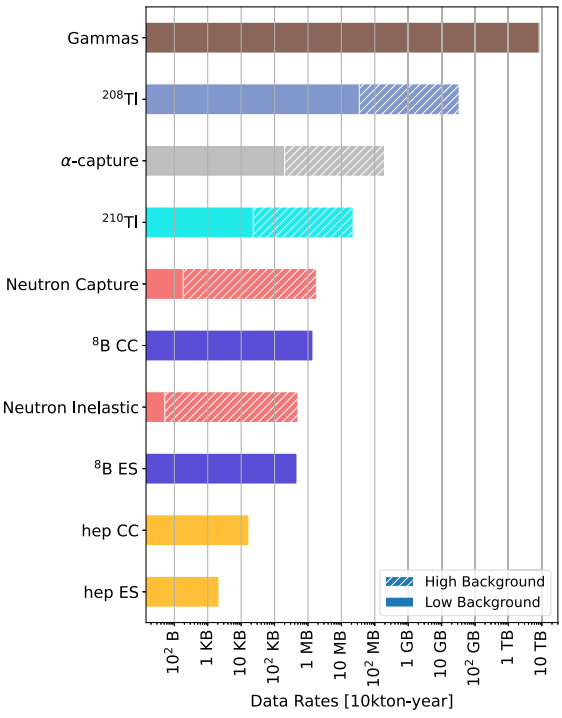

FIG. 14. Expected data rates with Q-Pix readout per kt · yr for solar neutrino signal events and background processes in the high-background scenario (full bar length) and low-background scenario (removing the hatched region) for a CT of 12 resets.

VII. CONCLUSIONS

We have studied the feasibility of solar neutrino detection using a LArTPC equipped with Q-Pix technology. Our study outlines the main challenges in detecting solar neutrinos that must be addressed by future large-scale noble element detectors, such as DUNE [106], SOLAIRE [107], and—with the due caveats pertaining to the change of target nucleus—XLZD [108].

Our analysis includes an extensive evaluation of potential background sources that could affect solar neutrino detection in an underground LArTPC detector. Despite the high rates of background events, the continuous and low-data rate Q-Pix readout allows to set an energy threshold for this study of 3 MeV, similar to that of SK and HK, and above those of JUNO, SNO+, and Borexino. Internal radioactive backgrounds originating from bulk argon and radon decays make it difficult to detect solar neutrinos below a deposited energy of 5 MeV, as background rates exceed signal rates by nearly 10 orders of magnitude.

Beta decays and γ rays from radioactive processes—including rare decay—create an irreducible background that exceeds the solar neutrino signal by 5 to 11 orders of magnitude, depending on the energy range. This conclusion remains unchanged even when accounting for unmodeled mitigation effects such as ion drift or including additional sources of radioactivity from detector components like readout support structures. Although a low-background scenario significantly reduces internal background rates, they still remain too high to enable the study of solar neutrinos below 5 MeV unless a powerful photon detection system is assumed.

Above 5 MeV, the dominant background sources are photons originating externally to the detector—which can only be mitigated through fiducial volume cuts—and photons generated by α-capture processes in argon. These α particles arise from radon decay chains and could be reduced in a low-background detector scenario, with further suppression possible using techniques like pulse shape discrimination.

However, the two primary background processes above 5 MeV are poorly constrained due to the limited availability

of measurements of γ fluxes in the detector cavern and α-capture cross sections on argon. We explored the possibility of isolating hep neutrinos and obtaining a high-statistics sample of ^{8}B neutrinos in a low-background scenario, provided that strict fiducialization and flash-coincidence techniques are employed to identify solar events. These allow to identify neutrino signals in the range [3.5–16.0] MeV of deposited energy. Nonetheless, any definitive conclusion regarding hep neutrino discovery or detailed ^{8}B neutrino studies depends critically on precise measurements of cavern γ-ray emission and the α-capture process.

If future measurements confirm that γ rates and α-capture processes fall within the assumed order of magnitude, we have shown that off-line analysis tools can significantly enhance the potential for solar neutrino studies in a LArTPC equipped with a pixelated continuous readout and an effective light detection system.

Finally, we emphasize the necessity of a continuous readout system for solar neutrino detection. As demonstrated throughout this study, the background rates—despite caveats in some assumptions—are so high that traditional triggering approaches in LArTPCs are unlikely to be viable. Q-Pix technology, which enables significantly reduced data rates, emerges as a strong candidate to support continuous readout capabilities essential for these studies.

ACKNOWLEDGMENTS

This material is based upon work supported by the U.S. Department of Energy, Office of Science, Office of High Energy Physics Awards No. DE-0000253485 and No. DE-SC0020065 and by the STFC Grant No. ST/W003945/1. S. K. is supported by the Ezoe Memorial Recruit Scholarship, Mitsui Group 350th Anniversary Project, ONE CAREER Inc. and PKSHA Technology Inc. G. R. and S. S.-R have received funding from the European Union's Horizon 2020 Research and Innovation program under GA No. 101004761. J. B. R. B. is supported by the Gordon and Betty Moore Foundation through Grant No. GBMF11565 [109]. O. S. is supported by the High Energy Physics Integrated Circuits Fellowship under Award No. DE-SC0022296.

DATA AVAILABILITY

The data that support the findings of this article are not publicly available. The data are available from the authors upon reasonable request.

[1] John N. Bahcall, M. H. Pinsonneault, and Sarbani Basu, Solar models: Current epoch and time dependences, neutrinos, and helioseismological properties, Astrophys. J. **555**, 990 (2001).
[2] D. B. Guenther, P. Demarque, Y. C. Kim, and M. H. Pinsonneault, Standard solar model, Astrophys. J. **387**, 372 (1992).
[3] Q. R. Ahmad *et al.* (SNO Collaboration), Direct evidence for neutrino flavor transformation from neutral-current interactions in the sudbury neutrino observatory, Phys. Rev. Lett. **89**, 011301 (2002).
[4] G. Aardsma *et al.*, A heavy water detector to resolve the solar neutrino problem, Phys. Lett. B **194**, 321 (1987).
[5] J. N. Abdurashitov *et al.*, Results from sage (the russian-american gallium solar neutrino experiment), Phys. Lett. B **328**, 234 (1994).
[6] L. Wolfenstein, Neutrino oscillations in matter, Phys. Rev. D **17**, 2369 (1978).
[7] Michele Maltoni and Alexei Yu. Smirnov, Solar neutrinos and neutrino physics, Eur. Phys. J. A **52**, 87 (2016).
[8] A. Gando *et al.* (KamLAND Collaboration), Reactor on-off antineutrino measurement with KamLAND, Phys. Rev. D **88**, 033001 (2013).
[9] Rasmi Hajjar, Sergio Palomares-Ruiz, and Olga Mena, Shedding light on the Δm212 tension with supernova neutrinos, Phys. Lett. B **854**, 138719 (2024).
[10] Sarbani Basu and H. M. Antia, Constraining solar abundances using helioseismology, Astrophys. J. Lett. **606**, L85 (2004).
[11] J. Montalbán, A. Miglio, A. Noels, N. Grevesse, and M. P. di Mauro, Solar model with CNO revised abundances, ESA Spec. Publ. **559**, 574 (2004), arXiv:astro-ph/0408055.
[12] J. W. Harvey *et al.*, The global oscillation network group (gong) project, Science **272**, 1284 (1996).
[13] John N. Bahcall, Solar models and solar neutrinos: Current status, Phys. Scr. T **121**, 46 (2005).
[14] L. Hüdepohl, B. Müller, H. T. Janka, A. Marek, and G. G. Raffelt, Neutrino signal of electron-capture supernovae from core collapse to cooling, Phys. Rev. Lett. **104**, 251101 (2010).
[15] G. Alimonti *et al.*, Science and technology of borexino: A real-time detector for low energy solar neutrinos, Astropart. Phys. **16**, 205 (2002).
[16] V. Albanese *et al.* (SNO+Collaboration), The SNO+ experiment, J. Instrum. **16**, P08059 (2021).
[17] M. Agostini *et al.* (BOREXINO Collaboration), Comprehensive measurement of pp-chain solar neutrinos, Nature (London) **562**, 505 (2018).
[18] M. Agostini *et al.* (Borexino Collaboration), First simultaneous precision spectroscopy of pp, ^{7}Be, and pep solar neutrinos with Borexino Phase-II, Phys. Rev. D **100**, 082004 (2019).

[19] M. Agostini *et al.* (Borexino Collaboration), Improved measurement of ^{8}B solar neutrinos with 1.5*kty* of Borexino exposure, Phys. Rev. D **101**, 062001 (2020).

[20] M. Agostini *et al.* (BOREXINO Collaboration), Experimental evidence of neutrinos produced in the CNO fusion cycle in the Sun, Nature (London) **587**, 577 (2020).

[21] D. Basilico *et al.* (BOREXINO Collaboration), Final results of Borexino on CNO solar neutrinos, Phys. Rev. D **108**, 102005 (2023).

[22] M. Anderson *et al.* (SNO+Collaboration), Measurement of the ^{8}B solar neutrino flux in SNO+ with very low backgrounds, Phys. Rev. D **99**, 012012 (2019).

[23] S. Fukuda *et al.*, The Super-Kamiokande detector, Nucl. Instrum. Methods Phys. Res., Sect. A **501**, 418 (2003).

[24] K. Abe *et al.* (Super-Kamiokande Collaboration), Solar neutrino measurements using the full data period of Super-Kamiokande-IV, Phys. Rev. D **109**, 092001 (2024).

[25] K. Abe *et al.* (Hyper-Kamiokande Collaboration), Hyper-Kamiokande design report, arXiv:1805.04163.

[26] Fengpeng An *et al.* (JUNO Collaboration), Neutrino physics with JUNO, J. Phys. G **43**, 030401 (2016).

[27] Angel Abusleme *et al.* (JUNO Collaboration), JUNO sensitivity to ^{7}Be, pep, and CNO solar neutrinos, J. Cosmol. Astropart. Phys. 10 (2023) 022.

[28] John N. Bahcall, M. Baldo-Ceolin, D. B. Cline, and C. Rubbia, Predictions for a liquid argon solar neutrino detector, Phys. Lett. B **178**, 324 (1986).

[29] Francesco Capozzi, Shirley Weishi Li, Guanying Zhu, and John F. Beacom, DUNE as the next-generation solar neutrino experiment, Phys. Rev. Lett. **123**, 131803 (2019).

[30] M. Antonello *et al.*, Operation and performance of the ICARUS-T600 cryogenic plant at Gran Sasso underground Laboratory, J. Instrum. **10**, P12004 (2015).

[31] R. Acciarri *et al.* (MicroBooNE Collaboration), Design and construction of the MicroBooNE detector, J. Instrum. **12**, P02017 (2017).

[32] Roberto Acciarri *et al.* (LArIAT Collaboration), The Liquid Argon In A Testbeam (LArIAT) experiment, J. Instrum. **15**, P04026 (2020).

[33] C. Anderson *et al.*, The ArgoNeuT detector in the NuMI low-energy beam line at Fermilab, J. Instrum. **7**, P10019 (2012).

[34] Serhan Tufanli (SBND Collaboration), The SBND experiment, Proc. Sci., HQL2016 (**2017**) 070.

[35] Babak Abi *et al.* (DUNE Collaboration), Deep Underground Neutrino Experiment (DUNE), Far detector technical design report, Volume II: DUNE physics, arXiv:2002.03005.

[36] Corey Adams, Marco Del Tutto, Jonathan Asaadi, Madeline Bernstein, Eric Church, Roxanne Guenette, Jairo M. Rojas, Hunter Sullivan, and Akshat Tripathi, Enhancing neutrino event reconstruction with pixel-based 3D readout for liquid argon time projection chambers, J. Instrum. **15**, P04009 (2020).

[37] R. Acciarri *et al.* (MicroBooNE Collaboration), Noise characterization and filtering in the MicroBooNE Liquid Argon TPC, J. Instrum. **12**, P08003 (2017).

[38] B. Abi, R. Acciarri, M. A. Acero, G. Adamov, D. Adams, M. Adinolfi *et al.* (DUNE Collaboration), Deep Underground Neutrino Experiment (DUNE), Far detector technical design report, Volume IV: Far detector single-phase technology, J. Instrum. **15**, T08010 (2020).

[39] Adam Abed Abud *et al.* (DUNE Collaboration), The DUNE far detector vertical drift technology. Technical design report, J. Instrum. **19**, T08004 (2024).

[40] D. A. Dwyer *et al.*, LArPix: Demonstration of low-power 3D pixelated charge readout for liquid argon time projection chambers, J. Instrum. **13**, P10007 (2018).

[41] Adam Abed Abud *et al.* (DUNE Collaboration), Highly-parallelized simulation of a pixelated LArTPC on a GPU, J. Instrum. **18**, P04034 (2023).

[42] N. Anfimov *et al.* (SoLAr Collaboration), First demonstration of a combined light and charge pixel readout on the anode plane of a LArTPC, J. Instrum. **19**, P11010 (2024).

[43] David Nygren and Yuan Mei, Q-Pix: Pixel-scale signal capture for Kiloton Liquid Argon TPC detectors: Time-to-charge waveform capture, local clocks, dynamic networks, arXiv:1809.10213.

[44] T. Bezerra *et al.*, Large low background kton-scale liquid argon time projection chambers, J. Phys. G **50**, 060502 (2023).

[45] Hamamatsu Photonics K. K., https://hamamatsu.su/files/uploads/pdf/3_mppc/s13370_vuv4-mppc_b_(1).pdf.

[46] M. Rooks, S. Abbaszadeh, J. Asaadi, M. Febbraro, R. W. Gladen, E. Gramellini, K. Hellier, F. Maria Blaszczyk, and A. D. McDonald, Development of a novel, windowless, amorphous selenium based photodetector for use in liquid noble detectors, J. Instrum. **18**, P01029 (2023).

[47] M. Rooks, S. Abbaszadeh, J. Asaadi, V. A. Chirayath, M. Febbraro, M. Á. García-Peris, E. Gramellini, K. Hellier, B. Sudarsan, and I. Tzoka, Characterization of lateral amorphous selenium photodetectors for low-photon and VUV detection at cryogenic temperatures, arXiv:2507.18497.

[48] F. Marinho (DUNE Collaboration), APEX: Optimized vertical drift PDS for DUNE FD3, J. Instrum. **20**, C05029 (2025).

[49] Peng Miao, Jonathan Asaadi, James B. R. Battat, Mikyung Han, Kevin Keefe, S. Kohani, Austin D. McDonald, David Nygren, Olivia Seidel, and Yuan Mei, Demonstrating the Q-pix front-end using discrete OpAmp and CMOS transistors, arXiv:2311.09568.

[50] S. Agostinelli *et al.*, Geant4—A simulation toolkit, Nucl. Instrum. Methods Phys. Res., Sect. A **506**, 250 (2003).

[51] Steven Gardiner, Simulating low-energy neutrino interactions with marley, Comput. Phys. Commun. **269**, 108123 (2021).

[52] C. Andreopoulos *et al.*, The genie neutrino monte carlo generator, Nucl. Instrum. Methods Phys. Res., Sect. A **614**, 87 (2010).

[53] S. Kubota *et al.* (Q-Pix Collaboration), Enhanced low-energy supernova burst detection in large liquid argon time projection chambers enabled by Q-Pix, Phys. Rev. D **106**, 032011 (2022).

[54] Martin Ester, Hans-Peter Kriegel, Jörg Sander, and Xiaowei Xu, A density-based algorithm for discovering clusters in large spatial databases with noise, in *Proceedings of the Second International Conference on Knowledge Discovery and Data Mining*, KDD'96 (AAAI Press, Portland, Oregon, 1996), pp. 226–231.

[55] T. Takahashi, M. Miyajima, S. Konno, T. Hamada, S. Kubota, H. Shibamura, and T. Doke, The w-value of liquid argon, Phys. Lett. **44A**, 123 (1973).
[56] B. Aharmim *et al.* (SNO Collaboration), Search for *hep* solar neutrinos and the diffuse supernova neutrino background using all three phases of the Sudbury Neutrino Observatory, Phys. Rev. D **102**, 062006 (2020).
[57] John N. Bahcall, Aldo M. Serenelli, and Sarbani Basu, New solar opacities, abundances, helioseismology, and neutrino fluxes, Astrophys. J. **621**, L85 (2005).
[58] P. Benetti *et al.* (WARP Collaboration), Measurement of the specific activity of ar-39 in natural argon, Nucl. Instrum. Methods Phys. Res., Sect. A **574**, 83 (2007).
[59] M. Agostini *et al.* (GERDA Collaboration), The background in the $0\nu\beta\beta$ experiment GERDA, Eur. Phys. J. C **74**, 2764 (2014).
[60] A. S. Barabash, R. R. Saakyan, and V. I. Umatov, On concentration of ^{42}Ar in the Earth's atmosphere, Nucl. Instrum. Methods Phys. Res., Sect. A **839**, 39 (2016).
[61] R. Ajaj *et al.* (DEAP Collaboration), Electromagnetic backgrounds and potassium-42 activity in the DEAP-3600 dark matter detector, Phys. Rev. D **100**, 072009 (2019).
[62] D. Caratelli *et al.*, Low-energy physics in neutrino LArTPCs, arXiv:2203.00740.
[63] P. Agnes *et al.* (DarkSide Collaboration), Results from the first use of low radioactivity argon in a dark matter search, Phys. Rev. D **93**, 081101 (2016); **95**, 069901(A) (2017).
[64] P. Agnes *et al.* (DarkSide-20k Collaboration), Separating ^{39}Ar from ^{40}Ar by cryogenic distillation with Aria for dark-matter searches, Eur. Phys. J. C **81**, 359 (2021), arXiv:2101.08686 [physics.ins-det].
[65] Sagar S. Poudel, Ben Loer, Richard Saldanha, Brianne R. Hackett, and Henning O. Back, Subsurface cosmogenic and radiogenic production of ^{42}Ar, Phys. Rev. D **110**, 082010 (2024).
[66] Kevin T. Lesko *et al.*, Deep underground science and engineering laboratory—Preliminary design report, arXiv:1108.0959.
[67] Jaret Heise, The sanford underground research facility at homestake, J. Phys. Conf. Ser. **606**, 012015 (2015).
[68] Y. D. Chan *et al.*, The "low-background construction of laboratories at the 4850 ft level davis campus," https://sanfordlab.org/news/low-background-construction-laboratories-4850-ft-level-davis-campus.
[69] International Atomic Energy Agency (IAEA), https://www.iaea.org/topics/spent-fuel-management/depleted-uranium.
[70] J. B. Albert *et al.* (EXO-200 Collaboration), Measurements of the ion fraction and mobility of α- and β-decay products in liquid xenon using the EXO-200 detector, Phys. Rev. C **92**, 045504 (2015).
[71] Alissa Erin Monte, Alpha radiation studies and related backgrounds in the DarkSide-50 detector, Ph.D. thesis, Massachusetts University, Amherst, 2018.
[72] C. E. Aalseth *et al.* (DarkSide-20k Collaboration), DarkSide-20k: A 20 tonne two-phase LAr TPC for direct dark matter detection at LNGS, Eur. Phys. J. Plus **133**, 131 (2018).
[73] R. Ajaj *et al.* (DEAP Collaboration), Search for dark matter with a 231-day exposure of liquid argon using DEAP-3600 at SNOLAB, Phys. Rev. D **100**, 022004 (2019).
[74] G. S. Foote, D. Branford, D. C. Weisser, N. Shikazono, R. A. I. Bell, and F. C. P. Huang, Alpha capture to the giant dipole resonances of 42ca, 44ca and 52cr, Nucl. Phys. **A263**, 349 (1976).
[75] Balraj Singh and Jun Chen, Nuclear data sheets for a = 43, Nucl. Data Sheets **126**, 1 (2015).
[76] Shawn Westerdale, https://github.com/shawest/neucbot.
[77] Jun Chen, Nuclear data sheets for $a = 40$, Nucl. Data Sheets **140**, 1 (2017).
[78] Sean Patrick MacMullin, Elastic and inelastic scattering of neutrons from neon and argon: Impact on neutrinoless double-beta decay and dark matter experimental programs, Ph.D. thesis, North Carolina University, 2013.
[79] C. D. Nesaraja and E. A. McCutchan, Nuclear data sheets for A = 41, Nucl. Data Sheets **133**, 1 (2016).
[80] John Cameron, Jun Chen, Balraj Singh, and Ninel Nica, Nuclear data sheets for A = 37, Nucl. Data Sheets **113**, 365 (2012).
[81] E. T. Jurney, J. W. Starner, J. E. Lynn, and S. Raman, Thermal-neutron capture by ^{14}N, Phys. Rev. C **56**, 118 (1997).
[82] Said F. Mughabghab, *Atlas of Neutron Resonances: Resonance Parameters and Thermal Cross Sections. Z=1-100* 5th ed. (Elsevier, San Diego, CA, 2006).
[83] M. Haffke, L. Baudis, T. Bruch, A. D. Ferella, T. Marrodán Undagoitia, M. Schumann, Y.-F. Te, and A. van der Schaaf, Background measurements in the Gran Sasso underground laboratory, Nucl. Instrum. Methods Phys. Res., Sect. A **643**, 36 (2011).
[84] D. S. Akerib *et al.*, Measurement of the gamma ray background in the davis cavern at the sanford underground research facility, Astropart. Phys. **116**, 102391 (2020).
[85] High Energy Gamma-Rays measurements in the SNO cavity, https://sno.phy.queensu.ca/str/SNO-STR-97-009.pdf.
[86] A. Agrawal *et al.* (AMoRE Collaboration), Background study of the AMoRE-pilot experiment, Astropart. Phys. **162**, 102991 (2024).
[87] YangPing Shen *et al.*, Measurement of gamma detector backgrounds in the energy range of 3–8 mev at Jinping underground laboratory for nuclear astrophysics, Sci. China Phys. Mech. Astron. **60**, 1869 (2017).
[88] C. E. Aalseth *et al.* (DarkSide-20k Collaboration), DarkSide-20k: A 20 tonne two-phase LAr TPC for direct dark matter detection at LNGS, Eur. Phys. J. Plus **133**, 131 (2018).
[89] C. W. Nahm and T. T. Thwaites, Radiative alpha capture by 38 Ar and 36 Ar, Nucl. Phys. **A103**, 503 (1967).
[90] N. G. Alenius *et al.*, Structure of 43Ca from the ^{40}Ar$(\alpha, n\gamma)^{43}$Ca reaction, Il Nuovo Cimento A (1965–1970) **8**, 147 (1972).
[91] Young Soo Yoon, Jungho Kim, and Hyeonseo Park, Neutron background measurement for rare event search experiments in the YangYang underground laboratory, Astropart. Phys. **126**, 102533 (2021).
[92] A. Abed Abud *et al.* (DUNE Collaboration), Design, construction and operation of the ProtoDUNE-SP Liquid Argon TPC, J. Instrum. **17**, P01005 (2022).

[93] B. J. Mount *et al.*, LUX-ZEPLIN (LZ) technical design report, arXiv:1703.09144.
[94] E. Aprile *et al.* (XENON Collaboration), The XENONnT dark matter experiment, Eur. Phys. J. C **84**, 784 (2024).
[95] P. A. Amaudruz *et al.* (DEAP-3600 Collaboration), Design and construction of the DEAP-3600 dark matter detector, Astropart. Phys. **108**, 1 (2019).
[96] Abdusalam Abdukerim *et al.* (PANDA-X Collaboration), PandaX-xT—A deep underground multi-ten-tonne liquid xenon observatory, Sci. China Phys. Mech. Astron. **68**, 221011 (2025).
[97] K. H. Ackermann *et al.* (GERDA Collaboration), The GERDA experiment for the search of $0\nu\beta\beta$ decay in ^{76}Ge, Eur. Phys. J. C **73**, 2330 (2013).
[98] D. S. Akerib *et al.*, Radiogenic and muon-induced backgrounds in the LUX dark matter detector, Astropart. Phys. **62**, 33 (2015).
[99] I. Barabanov, L. Bezrukov, E. Demidova, V. Gurentsov, S. Kianovsky, K. T. Knopfle, V. Kornouhkov, B. Schwingenheuer, and A. Vasenko, Shielding of the GERDA experiment against external gamma background, Nucl. Instrum. Methods Phys. Res., Sect. A **606**, 790 (2009).
[100] Marco Selvi, Study of the performances of the shield and muon veto of xenon1t, https://indico.in2p3.fr/event/1565/contributions/20488/attachments/16792/20571/Xenon1T-ExternalBackgrounds.pdf.
[101] International Atomic Energy Agency (IAEA), Thermal neutron capture γs (capgam) (2008), https://www-nds.iaea.org/capgam/index.htmlx.
[102] L. Meyer-Schützmeister, Z. Vager, R. E. Segel, and P. P. Singh, The giant dipole resonance excited by α-capture, Nucl. Phys. **A108**, 180 (1968).
[103] Shinzou Kubota, Masahiko Hishida, and Akira Nohara, Variation of scintillation decay in liquid argon excited by electrons and alpha particles, Nucl. Instrum. Methods **150**, 561 (1978).
[104] R. S. Raghavan, Inverse β^- decay of ^{40}Ar: A new approach for observing mev neutrinos from laboratory and astrophysical sources, Phys. Rev. D **34**, 2088 (1986).
[105] Babak Abi *et al.* (DUNE Collaboration), Deep Underground Neutrino Experiment (DUNE), Far detector technical design report, Volume I Introduction to DUNE, J. Instrum. **15**, T08008 (2020).
[106] B. Abi *et al.* (DUNE Collaboration), The DUNE far detector interim design report Volume 1: Physics, technology and strategies, arXiv:1807.10334.
[107] Darren Price, Solaire: A near-future vision for a direct dark matter and neutrino fog science experiment at the Boulby Underground Laboratory, https://indico.global/event/5610/contributions/44727/ (2024), presented at the Dark Matter UK (DMUK) Meeting, May 13, 2024.
[108] Laura Baudis, Darwin/xlzd: A future xenon observatory for dark matter and other rare interactions, Nucl. Phys. **B1003**, 116473 (2024).
[109] 10.37807/GBMF11565.